

A 2-D Non-Stationary GBSM for Vehicular Visible Light Communication Channels

Ahmed Al-Kinani, Jian Sun¹, *Member, IEEE*, Cheng-Xiang Wang², *Fellow, IEEE*,
Wensheng Zhang³, *Member, IEEE*, Xiaohu Ge⁴, *Senior Member, IEEE*,
and Harald Haas⁵, *Fellow, IEEE*

Abstract—In this paper, a new non-stationary regular-shaped geometry-based stochastic model (RS-GBSM) is proposed for vehicular visible light communications (V VLC) channels. The proposed model utilizes a combined two-ring model and a confocal ellipse model, in which the received optical power is constructed as a sum of single-bounced (SB) and double-bounced (DB) components, in addition to the line-of-sight (LoS) component. Using the proposed RS-GBSM, the channel impulse response is generated and utilized to investigate V VLC channel characteristics, such as channel gain and root-mean-square (RMS) delay spread. The received optical power is computed considering the distance between the optical transmitter (Tx) and the optical receiver (Rx). Moreover, the impact of the Rx height on the received power is considered for the LoS scenario. The results show that the LoS power highly depends on the distance, Rx height, and the optical source pattern. For the SB components, it is confirmed that the channel gain in dB and the RMS delay spread follow Gaussian distributions. Finally, the results indicate

that the detected optical power from the DB components is low enough to be overlooked.

Index Terms—Channel gain, RMS delay spread, RS-GBSM, vehicle-to-vehicle communications, visible light communications.

I. INTRODUCTION

WITH nearly 1.3 million people dying in road crashes yearly and in average 3,287 deaths per day, road traffic crashes become the ninth leading cause of death and account for 2.2% of all deaths globally [1]. Road traffic injuries are considered as the leading cause of death among young people at ages 15–29 [2] and the second leading cause of death worldwide among young people at ages 5–14. Unless action is taken, road traffic injuries are predicted to become the fifth leading cause of death by 2030 [1]. On the other hand, road crashes cost USD \$518 billion globally [3]. Consequently, many researches and projects have been conducted in order to get a better traffic system. Vehicular communication is an important and emerging area of research in the field of vehicular technology. The main objective of using this new technology is to create an accident-free environment. Vehicular networks would potentially have three main types of communications, i.e., road infrastructure-to-vehicle (R2V), vehicle-to-road infrastructure (V2R), and vehicle-to-vehicle (V2V) communications. The first two scenarios of communication enable the driver to access the Internet to get directions, road maps, congestions, and accidents in real time. On the other hand, V2V communications enable the cars to share the information with each other in order to exchange information that may be useful in facilitating road safety such as collision warning, lane departure, loss of stability, braking, speed, direction of travel and location. Recently, vehicular ad-hoc network (VANET) is an advanced network which mainly provides intelligent transportation systems (ITS) services to the end users to improve road safety and traffic efficiency. VANET uses dedicated short-range communications (DSRC)/wireless access in vehicular environments (WAVE) protocols for fast data communications.

In order to implement aforementioned standards, new hardware need to be added. However, adding more hardware to the infrastructures and cars is always an issue in terms of cost and power consumption. Therefore, the idea is to take advantage of visible light communications (VLC) technology in vehicular communications to introduce the so-called vehicular VLC (VVLC) [4]. VLC based on light-emitting diodes (LEDs)

Manuscript received November 28, 2017; revised July 16, 2018; accepted August 25, 2018. Date of publication October 9, 2018; date of current version December 10, 2018. This work was supported in part by the Natural Science Foundation of China under Grant 61771293, in part by the Shandong Provincial Natural Science Foundation under Grant ZR2017MF012, in part by the Key Research and Development Program of Shandong Province under Grant 2016GGX101014, in part by the Taishan Scholar Program of Shandong Province, in part by the Science and Technology Project of Guangzhou under Grant 201704030105, in part by the EU H2020 RISE TESTBED Project under Grant 734325, in part by the Hubei Provincial Science and Technology Department under Grant 2016AHB006, and in part by the Ministry of Higher Education and Scientific Research of Iraq under Grant 790. The associate editor coordinating the review of this paper and approving it for publication was R. He. (*Corresponding author: Cheng-Xiang Wang.*)

A. Al-Kinani was with the Institute of Sensors, Signals and Systems, School of Engineering and Physical Sciences, Heriot-Watt University, Edinburgh EH14 4AS, U.K. He is now with the Iraqi Ministry of Communications, Baghdad 10013, Iraq (e-mail: ahmed.alkinani@yahoo.com).

J. Sun and W. Zhang are with the Shandong Provincial Key Lab of Wireless Communication Technologies, School of Information Science and Engineering, Shandong University, Qingdao 266237, China (e-mail: sunjian@sdu.edu.cn; zhangwsh@sdu.edu.cn).

C.-X. Wang is with the National Mobile Communications Research Laboratory, School of Information Science and Engineering, Southeast University, Nanjing 210096, China, and also with the Institute of Sensors, Signals and Systems, School of Engineering and Physical Sciences, Heriot-Watt University, Edinburgh EH14 4AS, U.K. (e-mail: chxwang@seu.edu.cn).

X. Ge is with the School of Electronic Information and Communications, Huazhong University of Science and Technology, Wuhan 430074, China (e-mail: xhge@mail.hust.edu.cn).

H. Haas is with the School of Engineering, Institute of Digital Communications, The University of Edinburgh, Edinburgh EH9 3JL, U.K. (e-mail: h.haas@ed.ac.uk).

Color versions of one or more of the figures in this paper are available online at <http://ieeexplore.ieee.org>.

Digital Object Identifier 10.1109/TWC.2018.2873323

have attracted ever increasing attention, particularly for indoor wireless data transmission [5], [6]. Compared to conventional vehicular cellular systems, VVLC scenarios can be classified as a small spatial scale (SSS) communication scenario since the distance between the transmitter (Tx) and receiver (Rx) is smaller than 300 meters [7], [8]. In terms of infrastructure, cars already have LEDs such as front headlights, tail light, and wing mirror flasher that can be used for data transmission. At the receiving side, an ordinary camera-based receiver can act as an optical receiver. Most recently, the combination of the VLC technology with a camera is termed as optical camera communication (OCC) system [9]. The fact that new cars are equipped with cameras will pave the way for VVLC. For instance, the United States will require backup (rear view) cameras to be installed in new cars beginning in 2018. Furthermore, the transportation lighting infrastructure such as street lamps, traffic lights, variable message boards, etc., are changing to LEDs, which results in further cost reduction since no new infrastructure expense is required. On the other hand, this new technology is not a night technology as it would seem, since it can be used in daytime, especially after the road safety legislative requirements have been made. For instance, in 2008, European Commission adopted a legislation that all new cars will have to be equipped with daytime running lights (DRLs) [10]. DRLs are designed to come on automatically when the engine is started [11].

In this paper, we derive a new regular-shaped geometry-based stochastic model (RS-GBSM) for VVLC channels. In this model, the effective scatterers are located on regular shapes, namely, two rings and one confocal ellipse. A RS-GBSM is mathematically tractable and to the authors' knowledge, this is the first time that a RS-GBSM is proposed to investigate VVLC channel characteristics.

Overall, the major contributions and novelties of our work can be summarized as follows:

- 1) A new non-stationary RS-GBSM for VVLC channels is proposed. It considers the line-of-sight (LoS) component and the single-bounced (SB) rays that reflect off the effective scatterers located on the Tx-ring and the Rx-ring as well as the ellipse models. Furthermore, the proposed model considers the double-bounced (DB) rays that reflect off the effective scatterers located on both Tx-ring and Rx-ring models.
- 2) Based on the proposed RS-GBSM, the statistical properties of the VVLC channel are derived and thoroughly investigated, i.e., optical path lengths, optical received power, channel gain, mean excess delay, and root-mean-square (RMS) delay spread.
- 3) The scatterers are distributed uniformly on the Tx-ring, Rx-ring, and an ellipse where the Tx and the target vehicle are located at the foci. The impacts of the angle of departure (AoD) and angle of arrival (AoA) on the VVLC channels statistical properties are investigated thoroughly. Consequently, it is demonstrated that the distributions of the channel gain in dB and RMS delay spread for SB components follow Gaussian distribution.
- 4) Unlike existing models, the proposed RS-GBSM is able to model the DB rays. However, it is demonstrated

that the DB components carry inconsiderable optical power.

The rest of this paper is structured as follows. Section II presents the various existing VVLC channel models. Section III describes the proposed RS-GBSM for VVLC channels. The main VVLC channel characteristics are presented in Section IV. Simulation results and analysis are unveiled in Section V. Conclusions are finally drawn in Section VI.

II. EXISTING CHANNEL MODELS FOR VEHICULAR COMMUNICATIONS

For the sake of a VVLC link design and performance evaluation, detailed knowledge about the underlying propagation channel is indispensable. Therefore, channel modeling is the very first step for efficient, reliable, and robust communication systems design. The fundamental task of channel modeling is finding an approach to model the communication environment. In this context, RS-GBSMs have widely been used in conventional RF-based vehicular systems to model V2V channels [12]–[16]. In order to preserve the mathematical tractability, RS-GBSMs assume that all the effective scatterers are located on regular shapes such as rings, ellipses or a combination of these shapes in the case of two-dimensional (2D) channel modeling. Different from physical scatterers, effective scatterers may include several physical scatterers which are unresolvable in delay domain [14]. Although RS-GBSM approach is worthwhile even if the carrier frequency is different, channel knowledge obtained from conventional V2V based radio systems cannot be directly used for V2V based VLC systems. This is due to the fact that optical wireless channels do not experience multipath fading since the PD dimensions are in the order of millions of optical wavelengths, which provides an efficient spatial diversity that exhibits a high degree of immunity to multipath fading [17]. Furthermore, the use of intensity modulation/direct detection (IM/DD) scheme in VLC systems eliminates Tx and Rx oscillators and hence no frequency offset (FO) in VLC. On the other hand, regarding Doppler shift, it was shown that Doppler frequency has negligible effects in optical wireless communications (OWCs) systems [18]. This is because the corresponding wavelength shift is small enough to assume that bandwidth spreading and the signal-to-noise ratio (SNR) variation due to Doppler are insignificant problems in most IM/DD systems. Based on these facts, it can be concluded that there is no small-scale fading in VLC. However, VLC suffer from the effects of multipath dispersion, which manifests itself in a practical sense as ISI.

A considerable amount of work has been done based on VVLC in terms of R2V communication technology such as [19] and [20]. However, the previous work considered only the LoS channel between the Tx and Rx. Such a channel model is deterministically derived based on a specific scenario of application. In reality, however, the received signal contains other non-LoS (NLoS) components arriving from different paths due to multipath propagation. The latter components result from reflections off surrounding obstacles. Furthermore, a short while ago, a deterministic VVLC V2V and V2R channel models based on the ray-tracing method was

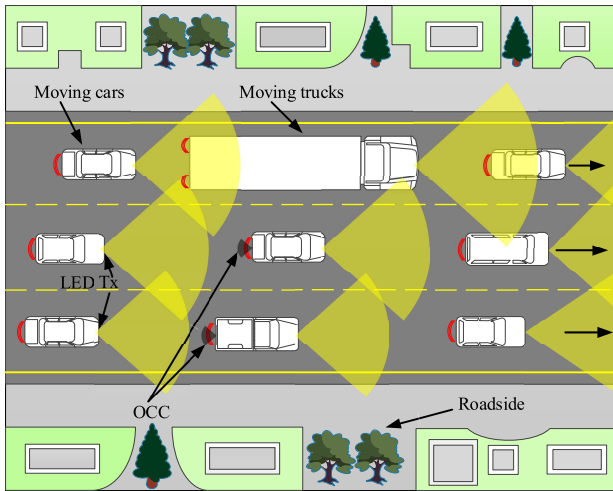


Fig. 1. Typical VVLC environments.

proposed in [21] and [22]. This type of channel modeling requires a detailed and time-consuming description of the propagation environment and consequently cannot be easily generalized to a wider class of scenarios. The authors in [23] used geometry-based road-surface reflection model, which considered LoS and SB components. The latter model ignored all other reflections except that reflected off the road-surface, i.e., the asphalt. On the other hand, RS-GBSM approach has been employed for indoor VLC channels. The authors in [24] used the one-ring model for investigating indoor VLC channel characteristics. While in [25], a combined two-ring and one ellipse model was proposed to model indoor VLC channels considering up to three reflections. A comprehensive survey of VLC channel measurements and models was provided in [26]. Most importantly, it is worth noting that the shortage of measurement-based channel models of VVLC, particularly for V2V scenarios, hinders the progress of IEEE 802.15.7 standardization since it does not discuss any channel parameter details that describe the reference channel model. Motivated by the above research gaps, in this paper we propose a new non-stationary RS-GBSM that addresses all the aforementioned shortcomings of the existing VVLC channel models.

III. VVLC CHANNEL MODEL

For vehicular VLC channels, there are three major elements should be modeled: the road traffic, the environment adjacent to the road, and the wave propagation between the vehicles. In terms of first and second elements, this paper considers a SSS VVLC system model deployed in a typical urban canyon as illustrated in Fig. 1. Here, the road environment includes dynamic road traffic, e.g., moving cars, vans, and trucks, and the roadside environment, e.g., buildings, parked cars, road signs, and trees. In terms of wave propagation between the Tx and the target vehicles, there are further two key elements should be modeled, namely, the Tx pattern and the Rx aperture size. In VVLC, the Tx is usually an automotive LED headlamp. Unfortunately, since VVLC technology is still

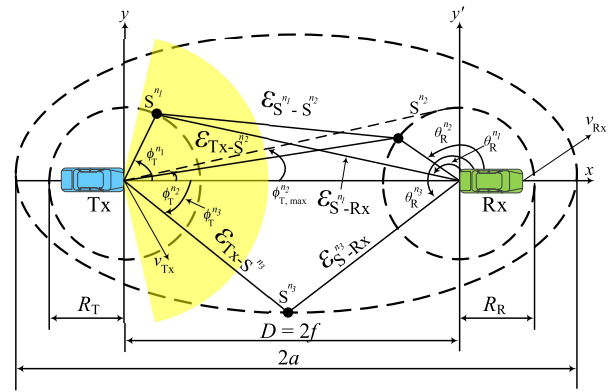


Fig. 2. A generic VVLC RS-GBSM combining a two-ring and a confocal ellipse model.

in very early stages of research, a standard headlamp with measured beam pattern model does not exist yet. Furthermore, the existing Halogen and gas discharge (Xenon) lamps are not suitable for intensity modulation purposes. Therefore, an ideal Lambertian model is employed in this work. The generalized Lambertian radiation pattern having uniaxial symmetry is given as [27]

$$R(\phi_T) = \frac{\alpha + 1}{2\pi} \cos^\alpha(\phi_T), \quad \phi_T \in [-\pi/2, \pi/2]. \quad (1)$$

Here, α is the mode number of the radiation pattern, which identifies the directionality of the optical source, while, ϕ_T is the angle of irradiance which is commonly denoted as the angle of departure (AoD). In this paper, the optical receiver is assumed to be a non-imaging PIN photodiode (PD), which is equipped at the rear end of the vehicle. The main reason for preferring PDs is due to the fact that the OCC experiences light flickering and provides low data rate compared to PD-based systems, which are widely used in VLC [9]. The PD can be modeled using its effective collection area $A_{R_{\text{eff}}}$, which is given as [27]

$$A_{R_{\text{eff}}} = \begin{cases} A_R \cos(\theta_R), & 0 \leq \theta_R \leq \Psi_{\text{FoV}} \\ 0, & \theta_R > \Psi_{\text{FoV}}. \end{cases} \quad (2)$$

Here, A_R is the area of the PD. Equation (2) indicates that only the radiation that received by the PD within PD's FoV Ψ_{FoV} will be detected. The angle of incidence is denoted as the angle of arrival (AoA). In terms of the optical wireless channel, Fig. 2 illustrates the geometry of the proposed RS-GBSM for VVLC channels. The geometry of the proposed model is a combination of a two-ring model and a confocal ellipse model considering a single- and double-bounce two-ring model, a single-bounce ellipse model, in addition to the LoS component. The probable optical paths and the definitions of key geometry parameters are presented in Table I and Table II, respectively.

In this study, the two-ring is proposed to model the scatterers surrounding the Tx and Rx, whereas the ellipse is proposed to take the stationary roadside environments into considerations. Suppose there are N_1 local scatterers around the Tx lying on a ring of radius R_T and the n_1 th ($n_1 = 1, \dots, N_1$) local

TABLE I
PROBABLE OPTICAL PATHS

Component	Optical Path	Distance
LoS	Tx→Rx	D
1- SB – 11	1- Tx→S ⁿ¹ → Rx	1- $R_T + \varepsilon_{S^{n1}-Rx}$
2- SB – 12	2- Tx→S ⁿ² → Rx	2- $\varepsilon_{Tx-S^{n2}} + R_R$
3- SB – 13	3- Tx→S ⁿ³ → Rx	3- $\varepsilon_{Tx-S^{n3}} + \varepsilon_{S^{n3}-Rx}$
DB – 11	Tx→S ⁿ¹ →S ⁿ² → Rx	$R_T + \varepsilon_{S^{n1}-S^{n2}} + R_R$

scatterer is denoted by S^{n1} . Similarly, assume there are N_2 local scatterers around the Rx lying on a ring of radius R_R and the n_2 th ($n_2 = 1, \dots, N_2$) local scatterer is denoted by S^{n2} . For the ellipse model, N_3 local scatterers lying on an ellipse and the n_3 th ($n_3 = 1, \dots, N_3$) local scatterer is denoted by S^{n3} . Ellipses sharing common foci, i.e., they are confocal. Here, the ellipse's foci coincide with the position of the Tx vehicle and target (Rx) vehicle. The lengths of the ellipse's semi-major axis and semi-minor axis are denoted by the parameters a and b , respectively (assuming $b < a$). Based on ellipse definition, the Tx-Rx distance is given as $D = 2f$ with f denoting the distance from the centre of the ellipse to a focus and the equality $a^2 = b^2 + f^2$ holds. The Tx and Rx are moving with speeds v_{Tx} and v_{Rx} in directions determined by the angles of motion γ_{Tx} and γ_{Rx} , respectively. At the Tx, the AoDs are denoted by ϕ_T^{n1} , ϕ_T^{n2} , and ϕ_T^{n3} . While at the effective scatterers side S^{n1} , S^{n2} , and S^{n3} the corresponding AoAs and AoDs are denoted by θ_S^{n1} , θ_S^{n2} , θ_S^{n3} , and ϕ_S^{n1} , ϕ_S^{n2} , ϕ_S^{n3} , respectively. On the other hand, the corresponding AoAs of the waves that impinge on the Rx, are designated by θ_R^{n1} , θ_R^{n2} , and θ_R^{n3} . In the literature, many different distributions have been proposed to characterize AoD ϕ_T^{ni} and AoA θ_R^{ni} , such as Gaussian and the von Mises distributions [13]. In this paper, an isotropic scattering around the rings and ellipse is characterized by a uniform distribution of the AoD ϕ_T^{ni} and AoA θ_R^{ni} .

Based on the proposed channel model, the channel impulse response (CIR) can be expressed as a superposition of the LoS and NLoS components, as

$$h(t) = h^{\text{LoS}}(t) + h^{\text{NLoS}}(t). \quad (3)$$

The complexity of calculating the CIR grows exponentially with the number of reflections k . Furthermore, according to [17], $\|h^k(t)\| \rightarrow 0$, $k \rightarrow \infty$, and consequently the channel impulse response can be estimated considering only the primary reflections. For example, indoor optical wireless channel measurements have been demonstrated that the third reflection can deliver no more 5% from the transmitted power in most scenarios [28]. Therefore, this work considers the CIR for only primary reflections, i.e., SB and DB as well as the LoS component. Consequently, (3) can be rewritten in more detail regarding the SB and DB components, as

$$h(t) = h^{\text{LoS}}(t) + \sum_{i=1}^I h^{\text{SB}_i}(t) + h^{\text{DB}}(t). \quad (4)$$

Here, $I = 3$ which means there are three subcomponents for SB rays, i.e., SB – 11 from the Tx-ring, SB – 12 from the Rx ring, and SB – 13 from the ellipse. For the sake of a more practical VVLC channel model, the following two criteria have been assumed. Firstly, we introduced the visibility function $V(\theta_R)$ at the Rx side, which indicates that only the scatterers that located within PD's FoV will be considered. Visibility function $V(\theta_R)$ can be expressed as a function of PD's FoV Ψ_{FoV} as

$$V(\theta_R) = \begin{cases} 1 & \text{if } 0 \leq \text{AoA } \theta_R \leq \Psi_{\text{FoV}} \\ 0 & \text{if } \text{AoA } \theta_R > \Psi_{\text{FoV}}. \end{cases} \quad (5)$$

Secondly, the i -th ray, in the double-bounce model, is always reflected off from a far scatterer to a near scatterer, relative to the optical receiver. Therefore, some i -bounced components are not necessarily to be considered making the proposed model more realistic and practical. The LoS, SB and DB channels within the proposed model will be more detailed in next subsections.

A. The LoS Link

In the proposed model, if the Tx and Rx are stationary, the LoS component of the CIR is deterministic and given as a function of signal propagation delay between the Tx and Rx as [29]

$$h^{\text{LoS}}(t) = \frac{(\alpha + 1)A_R V(\theta_R)}{2\pi(D)^2} \cos^\alpha(\phi_T^{\text{LoS}}) \times \cos(\theta_R^{\text{LoS}}) \delta\left(t - \frac{D}{c}\right). \quad (6)$$

Here, $\delta(\cdot)$ refers to the Dirac delta function. However, if the Tx and Rx are moving, (6) can be rewritten as

$$h^{\text{LoS}}(t) = \frac{(\alpha + 1)A_R V(\theta_R)}{2\pi(D(t)_{\text{TR}})^2} \cos^\alpha(\phi_T^{\text{LoS}}) \times \cos(\theta_R^{\text{LoS}}) \delta\left(t - \frac{D(t)_{\text{TR}}}{c}\right) \quad (7)$$

where

$$D(t)_{\text{TR}} = \varepsilon(t)_{\text{TR}} - [\varepsilon(t)_{\text{Tx}} - \varepsilon(t)_{\text{Rx}}], \quad v_{\text{Tx}} > v_{\text{Rx}}. \quad (8)$$

Here, $D(t)_{\text{TR}}$ determines the time-varying distance between the Tx and the target Rx. While, $\varepsilon(t)_{\text{TR}}$, $\varepsilon(t)_{\text{Tx}}$, and $\varepsilon(t)_{\text{Rx}}$ are the initial Tx-Rx distance, Tx distance, and Rx distance, respectively. If the Tx and Rx are moving with speeds v_{Tx} and v_{Rx} in directions determined by the angles of motion γ_{Tx} and γ_{Rx} , then the distances $\varepsilon(t)_{\text{Tx}}$ and $\varepsilon(t)_{\text{Rx}}$, can be given as $\varepsilon(t)_{\text{Tx}} = v_{\text{Tx}} \times t \times \cos(\gamma_{\text{Tx}})$ and $\varepsilon(t)_{\text{Rx}} = v_{\text{Rx}} \times t \times \cos(\gamma_{\text{Rx}})$, respectively.

B. Single-Bounce Link

1) *Single-Bounce Channel in Two-Ring Model*: The first probable optical path within the two-ring model is SB – 11. The AoD of the n th transmitted wave is denoted by ϕ_T^{n1} , and the corresponding AoA is described by θ_R^{n1}

TABLE II
DEFINITIONS OF KEY GEOMETRY PARAMETERS

D	distance between the center of the Tx-ring and the center of the Rx-ring
T_R, R_R	radius of the Tx-ring and Rx-ring, respectively
a, b	semi-major axis and semi-minor axis of the ellipse, , respectively
$\phi_T^{(n_i)}$ ($i = 1, 2, 3$)	angle of departure (AoD) of the waves that emitted from the optical source
$\theta_R^{(n_i)}$ ($i = 1, 2, 3$)	angle of arrival (AoA) of the waves that impinge the optical receiver
$\theta_S^{(n_i)}$ ($i = 1, 2, 3$)	angle of arrival (AoA) of the waves that impinge the effective scatterers
$\phi_S^{(n_i)}$ ($i = 1, 2, 3$)	angle of departure (AoD) of the waves that reflecting off walls the effective scatterers
γ_{Tx}, γ_{Rx}	moving directions of the Tx and Rx in the x-y plane, respectively
v_{Tx}, v_{Rx}	velocities of the Tx and Rx, respectively
$\varepsilon_{Tx-S^{n_i}}$	distances from the Tx to scatterers n_i , ($i = 1, 2, 3$)
$\varepsilon_{S^{n_i}-Rx}$	distances from scatterers n_i to the Rx, ($i = 1, 2, 3$)
$\varepsilon_{S^{n_1}-S^{n_2}}$	distances from scatterer n_1 to scatterer n_2

($n_1 = 1, 2, \dots, N_1$). The SB component of the CIR for link SB – 11 can be written as

$$h_{Tx-Ring}^{SB}(t) = \sum_{n_1=1}^{N_1} \frac{(\alpha+1) V(\theta_R)}{2\pi(R_T)^2} \cos^\alpha(\phi_T^{n_1}) \cos(\theta_S^{n_1}) \times \frac{(\alpha+1) A_R \rho_{Vehicles}}{2\pi(\varepsilon_{S^{n_1}-Rx})^2} \cos^\alpha(\phi_S^{n_1}) \cos(\theta_R^{n_1}) \times \delta(t - \frac{\varepsilon_{S^{n_1}-Rx} + R_T}{c}). \quad (9)$$

Similarly, the SB component of the CIR for link SB – 12 can be written as

$$h_{Rx-Ring}^{SB}(t) = \sum_{n_2=1}^{N_2} \frac{(\alpha+1) V(\theta_R)}{2\pi(\varepsilon_{Tx-S^{n_2}})^2} \cos^\alpha(\phi_T^{n_2}) \cos(\theta_S^{n_2}) \times \frac{(\alpha+1) A_R \rho_{Vehicles}}{2\pi(R_R)^2} \cos^\alpha(\phi_S^{n_2}) \cos(\theta_R^{n_2}) \times \delta(t - \frac{\varepsilon_{Tx-S^{n_2}} + R_R}{c}). \quad (10)$$

Here, $\rho_{Vehicles}$ denotes the reflection coefficient of the vehicles body. The angle $\phi_{T,max}^{n_2}$ in Fig. 2 designates the maximum AoD $\phi_T^{n_2}$ that can be seen by the Rx. This quantity is related to R_R and D by $\phi_{T,max}^{n_2} = \arctan(R_R/D)$. From Fig. 2 and based on the application of the law of cosines in appropriate triangles, we get

$$\varepsilon_{S^{n_1}-Rx} = \sqrt{(R_T)^2 + (D_0)^2 - 2R_T D_0 \cos(\phi_T)} \quad (11)$$

and

$$\varepsilon_{Tx-S^{n_2}} = \sqrt{(R_R)^2 + (D_0)^2 - 2R_T D_0 \cos(\theta_R)}. \quad (12)$$

Note that the AoD and AoA are correlated for SB rays in the proposed model. Therefore, using the law of sines in appropriate triangles, we get

$$\theta_R = \arcsin\left[\frac{R_T \sin(\phi_T)}{\varepsilon_{S^{n_1}-Rx}}\right] \quad (13)$$

and

$$\phi_T = \arcsin\left[\frac{R_R \sin(\theta_R)}{\varepsilon_{Tx-S^{n_2}}}\right]. \quad (14)$$

Equations (13) and (14) are valid for links SB-11 and SB-12, respectively.

Hence, (11) can be rewritten as

$$\varepsilon_{S^{n_1}-Rx} = \sqrt{(R_T)^2 + (D_0)^2 - 2R_T D_0 \sqrt{1 - \left(\frac{R_T \sin(\theta_R)}{\varepsilon_{Tx-S^{n_1}}}\right)^2}}. \quad (15)$$

2) *Single-Bounce Channel in Ellipse Model*: According to the proposed model, there is one more probable optical path through the ellipse model, i.e., link SB – 13. The SB component of the CIR for link SB – 13 can be written as

$$h_{Ellipse}^{SB}(t) = \sum_{n_3=1}^{N_3} \frac{(\alpha+1) V(\theta_R)}{2\pi(\varepsilon_{Tx-S^{n_3}})^2} \cos^\alpha(\phi_T^{n_3}) \cos(\theta_S^{n_3}) \times \frac{(\alpha+1) A_R \rho_{Roadside}}{2\pi(\varepsilon_{S^{n_3}-Rx})^2} \cos^\alpha(\phi_S^{n_3}) \cos(\theta_R^{n_3}) \times \delta(t - \frac{\varepsilon_{Tx-S^{n_3}} + \varepsilon_{S^{n_3}-Rx}}{c}). \quad (16)$$

Here, $\rho_{Roadside}$ denotes the reflection coefficient of the roadside substances.

The optical path lengths through the ellipse model can be determined based on aforementioned ellipse properties. The total optical path through the ellipse model is

$$\varepsilon_{Tx-S^{n_3}} + \varepsilon_{S^{n_3}-Rx} = 2a \quad (17)$$

According to the law of cosines in triangle Tx – S^{n_3} – Rx, the optical path length between the Tx and a scatterer located on the ellipse, can be given as

$$\varepsilon_{Tx-S^{n_3}} = \sqrt{(\varepsilon_{S^{n_3}-Rx})^2 + (2f)^2 - 2(\varepsilon_{S^{n_3}-Rx})(2f) \cos(\theta_R^{n_3})}. \quad (18)$$

After doing some manipulation based on pure ellipse properties, we can get the relation between the path length and the AoA $\theta_R^{n_3}$, as

$$\varepsilon_{Tx-S^{n_3}} = \frac{a^2 + f^2 + 2af \cos(\theta_R^{n_3})}{a + f \cos(\theta_R^{n_3})}. \quad (19)$$

Substituting (19) to (17), we get

$$\varepsilon_{S^{n_3}-Rx} = \frac{b^2}{a + f \cos(\theta_R^{n_3})}. \quad (20)$$

Applying the law of sines to the triangle $\text{Tx} - S^{n_3} - \text{Rx}$ so as to find the relationship between the AoA $\theta_{\text{R}}^{n_3}$ and AoD $\phi_{\text{T}}^{n_3}$ for ellipse scattering region, we get

$$\phi_{\text{T}}^{n_3} = \arcsin\left[\frac{b^2 \sin(\theta_{\text{R}}^{n_3})}{a^2 + f^2 + 2af \cos(\theta_{\text{R}}^{n_3})}\right] \quad (21)$$

and

$$\phi_{\text{T}}^{n_3} = \arccos\left[\frac{2af + (a^2 + f^2) \cos(\theta_{\text{R}}^{n_3})}{a^2 + f^2 + 2af \cos(\theta_{\text{R}}^{n_3})}\right]. \quad (22)$$

For single-bounce in the two-ring model and the ellipse model, due to the microscopic irregularities of the scatterers surfaces, the reflection pattern is assumed to be diffuse and hence the reflected components can correctly be approximated using the Lambertian reflection pattern. This model states that the total radiant power observed from a Lambertian surface is directly proportional to the cosine of the angle between the observer's line-of-sight and the surface normal. At scatterers' surfaces, since there is no unique reference surface normal that we can refer to, we assumed that the surface normal angles are uniformly distributed over $[\phi_{\text{T}}^{n_i}, \theta_{\text{R}}^{n_i}]$. Hence, the scattering angles can be characterized as the following criterion

$$\phi_{\text{T}}^{n_i} > \theta_{\text{S}}^{n_i}, \phi_{\text{S}}^{n_i} > \theta_{\text{R}}^{n_i}, \quad i = 1, 2, 3. \quad (23)$$

Accordingly, the angles pairs $\theta_{\text{S}}^{n_1}, \phi_{\text{S}}^{n_1}, \theta_{\text{S}}^{n_2}, \phi_{\text{S}}^{n_2}, \theta_{\text{S}}^{n_3},$ and $\phi_{\text{S}}^{n_3}$ can be obtained by using trigonometry in triangles $\text{Tx} - S^{n_1} - \text{Rx}$, $\text{Tx} - S^{n_2} - \text{Rx}$, and $\text{Tx} - S^{n_3} - \text{Rx}$, respectively. For instance, according to trigonometry in Tx-ring model, if $\phi_{\text{T}}^{n_1}$ and $\theta_{\text{R}}^{n_1}$ have been determined as detailed previously, the third angle, i.e., the apex angle in the triangle $\text{Tx} - S^{n_1} - \text{Rx}$ can be determined accordingly. Hence, if $\theta_{\text{S}}^{n_1}$ is assumed as uniformly distributed, $\phi_{\text{S}}^{n_1}$ represents the complementary angle the of the apex in the triangle $\text{Tx} - S^{n_1} - \text{Rx}$. The same procedure is applied to determine $\theta_{\text{S}}^{n_2}, \phi_{\text{S}}^{n_2}, \theta_{\text{S}}^{n_3},$ and $\phi_{\text{S}}^{n_3}$.

It is worth to notice that unlike in LoS scenario, in SB scenario, the shortest optical paths are not necessarily carry more power than other paths as will be noticed in Section V. This is due to the effect of AoA and AoD at the scatterers.

C. Double-Bounce Link

In the DB scenario, the received power mainly comes from the DB rays which are reflected twice, firstly at Tx-ring and then at the Rx-ring. The DB components within combined two-ring and confocal ellipse model, i.e., the optical paths $\text{Tx} - S^{n_1} - S^{n_3} - \text{Rx}$ and $\text{Tx} - S^{n_3} - S^{n_2} - \text{Rx}$ are ignored since they reflect less power compared to the two-ring model as reported in [25]. This is due to the longer path length and lower reflectivity ρ_{Roadside} of the roadside scatterers. The DB component of the CIR in the two-ring model can be expressed as

$$\begin{aligned} h^{\text{DB}}(t) &= \sum_{n_1, n_2=1}^{N_1, N_2} \frac{(\alpha + 1) V(\theta_{\text{R}}) \cos^{\alpha}(\phi_{\text{T}}^{n_1}) \cos(\theta_{\text{S}}^{n_1})}{2\pi(R_{\text{T}})^2} \\ &\times \frac{(\alpha + 1) \cos^{\alpha}(\phi_{\text{S}}^{n_1}) \cos(\theta_{\text{S}}^{n_2}) \rho_{\text{Vehicles}}}{2\pi(\varepsilon_{\text{S}^{n_1} - \text{S}^{n_2}})^2} \\ &\times \frac{(\alpha + 1) \cos^{\alpha}(\phi_{\text{S}}^{n_2}) \cos(\theta_{\text{R}}^{n_2}) A_{\text{R}} \rho_{\text{Vehicles}}}{2\pi(R_{\text{R}})^2} \\ &\times \delta\left(t - \frac{D_{\text{DB}}}{c}\right) \end{aligned} \quad (24)$$

From the quadrilateral $\text{Tx} - S^{n_1} - S^{n_2} - \text{Rx}$, the distances D_{DB} and $\varepsilon_{\text{S}^{n_1} - \text{S}^{n_2}}$ can be expressed as

$$D_{\text{DB}} = T_{\text{R}} + \varepsilon_{\text{S}^{n_1} - \text{S}^{n_2}} + R_{\text{R}} \quad (25)$$

and

$$\begin{aligned} (\varepsilon_{\text{S}^{n_1} - \text{S}^{n_2}})^2 &= (\varepsilon_{\text{S}^{n_1} - \text{Rx}})^2 + (R_{\text{R}})^2 \\ &\quad - 2(\varepsilon_{\text{S}^{n_1} - \text{Rx}})R_{\text{R}} \cos(\theta_{\text{R}}^{n_1} - \theta_{\text{R}}^{n_2}). \end{aligned} \quad (26)$$

In the DB model, the AoA $\theta_{\text{S}}^{n_i}$ and the AoD $\phi_{\text{S}}^{n_i}$ ($i = 1, 2$) at an effective scatterer, have been determined by using the distances $\varepsilon_{\text{S}^{n_1} - \text{Rx}}$ and $\varepsilon_{\text{Tx} - \text{S}^{n_2}}$, in (11) and (12), respectively. For example, to compute $\theta_{\text{S}}^{n_1}$ and $\phi_{\text{S}}^{n_1}$ angles in Tx-ring, we use the law of cosines to determine the summit angle of the triangle $\text{Tx} - S^{n_1} - S^{n_2}$ with help of (12). Hence, if $\theta_{\text{S}}^{n_1}$ is assumed as uniformly distributed, $\phi_{\text{S}}^{n_1}$ represents the complementary angle of the apex in the triangle $\text{Tx} - S^{n_1} - S^{n_2}$. The same procedure is applied to determine $\theta_{\text{S}}^{n_2}$ and $\phi_{\text{S}}^{n_2}$ in Rx-ring by using law of cosines in triangle $S^{n_1} - S^{n_2} - \text{Rx}$ with help of (11).

IV. VVLC CHANNEL CHARACTERISTICS

A. VVLC Channel DC Gain

For OWCs, channel effect is completely characterized by the CIR $h(t)$ [30]. Once calculated, CIR can be used to analyze or simulate the effect of the optical wireless channel on the performance of OWC systems. For intensity-in, intensity-out channels, the zero-frequency (DC) value of their frequency responses can be expressed as [29]

$$H(0) = \int_{-\infty}^{\infty} h(t) dt. \quad (27)$$

The latter expression is referred as channel DC gain, which is the fraction of power emitted from a continuous-wave transmitter that is detected by the receiver. The channel gain in dB is given as [31]

$$\text{Optical gain(dB)} = -10 \log_{10} H(0). \quad (28)$$

B. Received Optical Power

According to the proposed model, the total received optical power can be generally expressed as

$$P_{\text{Rx}} = P_{\text{Tx}} [H(0)^{\text{LoS}} + H(0)^{\text{SB}} + H(0)^{\text{DB}}]. \quad (29)$$

In terms of transmitted power P_{Tx} , since a standard LEDs headlamp with measured beam pattern model is not available, we considered the luminous intensity I (cd) at 50% (median) of the low-beam tungsten-halogen headlamp. The isocandela diagram for a pair of low-beam tungsten-halogen headlamps is plotted in Fig. 3 [32]. Also, we consider the luminous efficacy of radiation (LER) of a high power phosphor-coated WLED to be 250.3 lm/W [23]. Thus the received optical power can be expressed as

$$P_{\text{Rx}} = \frac{I}{\text{LER}} [H(0)^{\text{LoS}} + H(0)^{\text{SB}} + H(0)^{\text{DB}}]. \quad (30)$$

Here, P_{Rx} represents the total received optical power from both LoS and NLoS components.

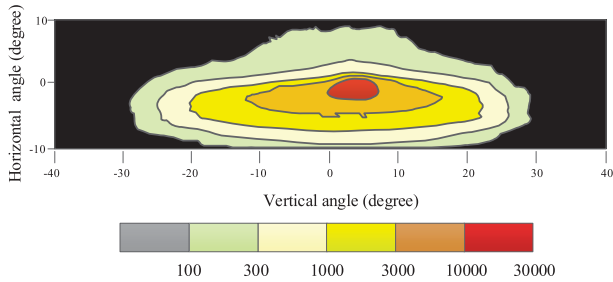


Fig. 3. Isocandela diagram of the median luminous intensities for a pair of low-beam tungsten-halogen headlamps [32].

TABLE III

MODEL PARAMETERS USED IN COMPUTER SIMULATIONS

Model Parameters	
The initial Tx-Rx distance	70 m
Semi-major axis a , semi-minor axis b	36.5 m, 10 m
Ring Radius (R_T, R_R)	3 m
Tx speed v_{Tx}	21.6 km/h
Rx speed v_{Rx}	14.4 km/h
Lane width	3.5 m [36]
Roadside width	2.2 m [37]
Vehicles Reflectivity ($\rho_{Vehicles}$)	0.8 [38]
Roadside Reflectivity ($\rho_{Roadside}$)	0.4 [39]
Luminous intensity (I)	7000 cd
Mode Number (α)	1
PD's Area	1 cm ²
PD's FoV	80°
Number of Scatterers	40 [33]

C. VVLC Channel RMS Delay Spread

Due to multipath reflection, the received signal appears as a sum of weighted, delayed copies of the transmitted signal [33]. Hence, wireless optical multipath channel stretches the transmitted signal in time resulting in the so-called temporal dispersion. This major characteristic can be quantified by the RMS delay spread D_{rms} of the CIR $h(t)$ as [34]

$$D_{rms} = \sqrt{\frac{\int_{-\infty}^{\infty} (t - \mu_{\tau})^2 h^2(t) dt}{\int_{-\infty}^{\infty} h^2(t) dt}} \quad (31)$$

where μ_{τ} is the mean excess delay: $\mu_{\tau} = \frac{\int_{-\infty}^{\infty} t h^2(t) dt}{\int_{-\infty}^{\infty} h^2(t) dt}$. Temporal dispersion directly determines the bandwidth of the optical wireless channel, where the maximum bit rate $R_b \leq 1/10D_{rms}$ [35]. Furthermore, multipath dispersion will set the limit on the symbol length that can be used in order to avoid intersymbol interference (ISI) [17].

V. RESULTS AND DISCUSSIONS

For simulation purposes, the entries of the environment parameters are summarized in Table III. The initial Tx-Rx distance is assumed to be 70 m. Note that the Tx and the target vehicle are assumed to be located at the foci of the ellipse. Therefore, according to the geometrical properties of the ellipse, the semi-major axis is half of the major axis,

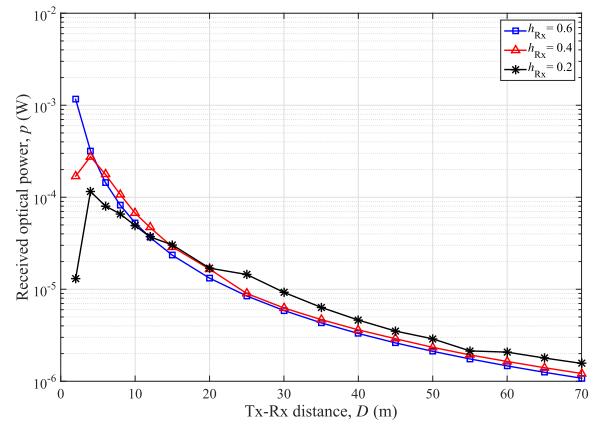


Fig. 4. Received optical power, $h_{Rx} = 0.2$ m, 0.4 m, and 0.6 m.

i.e., 36.5 m. While the semi-minor axis is assumed as 10 m to be suitable with lane width. In order to ensure safe driving, the minimum distance between the Tx vehicle or Rx vehicle and a scatterer is set as 1.5 m, which makes Tx and Rx rings' radius as 3 m. In terms of luminous intensity I , it is assumed to be 7000 cd, at 50% (median) of the low-beam tungsten-halogen headlamp [32]. The body of the vast majority of vehicles is made from steel. Therefore, average painted steel reflectance $\rho_{Vehicles}$ was considered. Likewise, for roadside environments, average concrete reflectance $\rho_{Roadside}$ was selected. According to [33], the reasonable value of N is in the range from 40 to 50. Furthermore, the standard values are assumed for other model parameters such as PD's area, PD's FoV, and mode number [17]. The most important VVLC channel characteristics are studied in the following subsections.

A. Received Optical Power

Let us assume that both the Tx and the Rx are moving in the same direction, i.e., $\gamma_{Tx} = \gamma_{Rx} = 0$, but in different speeds, e. g., $v_{Tx} = 6$ m/s and $v_{Rx} = 4$ m/s which correspond to 21.6 km/h and 14.4 km/h, respectively. Note that the speeds were chosen to be within urban speed limits. In terms of the LoS component and according to (6) and (30), the received optical power for different distances between the Tx and Rx is presented in Fig. 4. Here, we consider three different cases in which the PD is mounted at different heights h_{Rx} , i.e., 0.6 m, 0.4 m and 0.2 m. The Tx is mounted at a 0.6 m height, which is considered as the reference height. Note that in the first case, the Tx and the Rx are on the same plane, while there are 0.2 m and 0.4 m differences in the second and third cases, respectively. Referring to Fig. 4, we can highlight the following. The results show that in general the received power decreases as the distance increases, which is a intuitive behaviour. But in terms of the impact of PD position, it can be noticed that the received power is higher as Tx-Rx height difference increases. This is valid for Tx-Rx distances longer than 20 m. However, before this, since the Tx-Rx distances become shorter, the effects of both PD height and the observation angle with respect to PD's surface normal are considered as the direct result of changes in the received power. We can also clearly observe that the received power

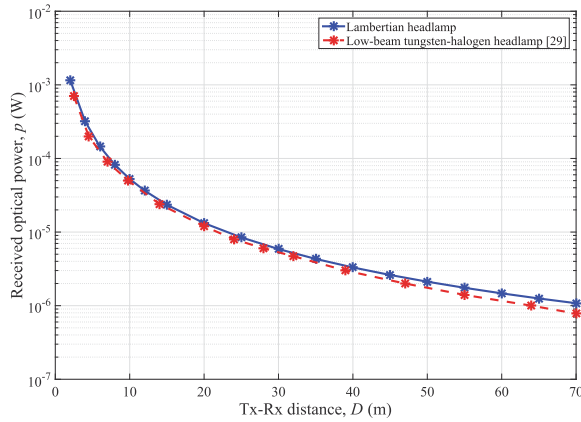


Fig. 5. Received optical power considering Lambertian headlamp and low-beam tungsten-halogen headlamp $h_{Rx} = 0.6$ m.

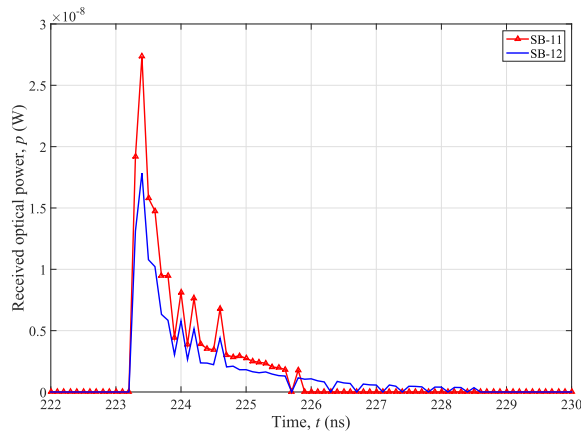


Fig. 6. Received power from SB – 11 and SB – 12 components within the two-ring model ($t = 0$, $D = 70$ m).

displays peaks at very short distance, specifically at 2 m, when there is height difference between the Tx and Rx, i.e., at 0.2 m and 0.4 m. This can be explained with the help of Fig. 3, where lower luminous intensities (cd) is obtained due to the effect of the higher vertical angles. For validation purposes, the simulation results based on Lambertian pattern showed a good agreement with those obtained by measurements based on using a low-beam tungsten-halogen headlamp in [32], as illustrated in Fig. 5. Here we assumed that both the Tx and Rx are mounted at a 0.6 m height.

On the other hand, in terms of SB components, the received power from SB – 11 and SB – 12 components of the two-ring model can be obtained by applying (9) and (10), respectively, as shown in Fig. 6. Here, we deliberately use the time-domain to indicate SB components of the CIR for the proposed channel model. It can be noticed, firstly, that the SB – 11 component carries more power than the SB – 12 components. This is due to the PD's FoV constraint, which states that all the scatterers are within PD's FoV. Secondly, the SB – 12 component has a longer tail compared with SB – 11 because of the wider aperture of the optical source at the Tx side. Furthermore, according to the proposed model, the last probable SB components are caused by the surrounding roadside

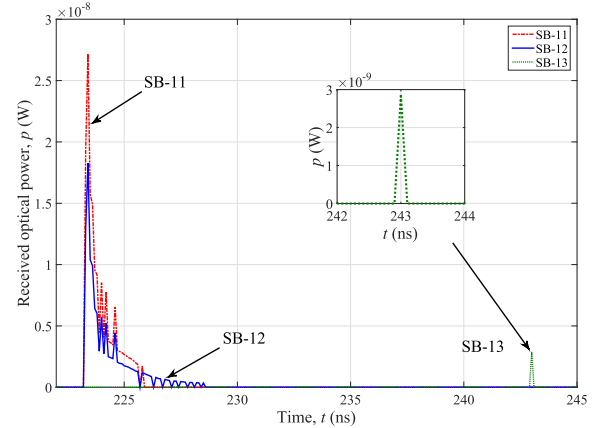


Fig. 7. Received power from SB – 11, SB – 12, and SB – 13 components within the combined two-ring and confocal ellipse model ($t = 0$, $D = 70$ m).

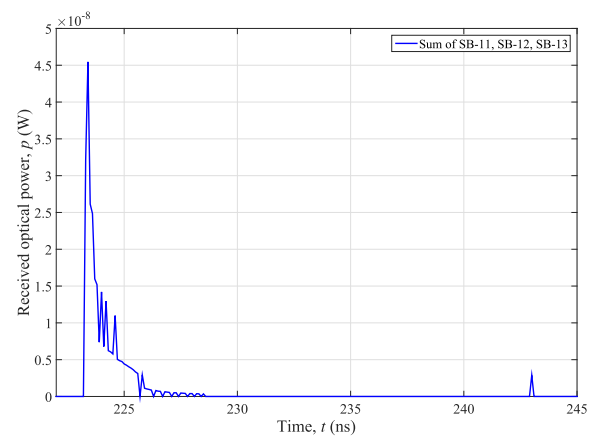


Fig. 8. Total received power from the combined two-ring and confocal ellipse models ($t = 0$, $D = 70$ m).

environments which are represented by the confocal ellipse model. According to (16), the received power of SB – 13 component is illustrated in Fig. 7, alongside SB – 11 and SB – 12 components. It can be observed that the received power from SB – 13 is significantly lower as compared to SB – 11 and SB – 12. This is due to two main factors: first, in the ellipse model the optical rays travel longer distance than their equivalents in the two-ring model and hence higher path loss. This also explains why SB – 13 comes later than the other first two components. Second, since we assumed that $\rho_{Roadside}$ represents the average of concrete reflectance, a high portion of the incident power will be absorbed due to the low concrete reflectivity. Simulation results in Fig. 7 can explain the effects of optical path lengths in addition to losses at the scatterers surfaces on the received optical power. In summary, longer optical path length and lower reflectivity can reduce the received signal strength. Consequently, the total power carried by SB components of the combined two-ring and confocal ellipse model is illustrated in Fig. 8. It is the sum of the power carried by SB – 11 and SB – 12, and SB – 13.

In terms of the DB component of the CIR, the received power which is obtained by applying (24) is presented in Fig. 9. Here, the simulation results have been obtained

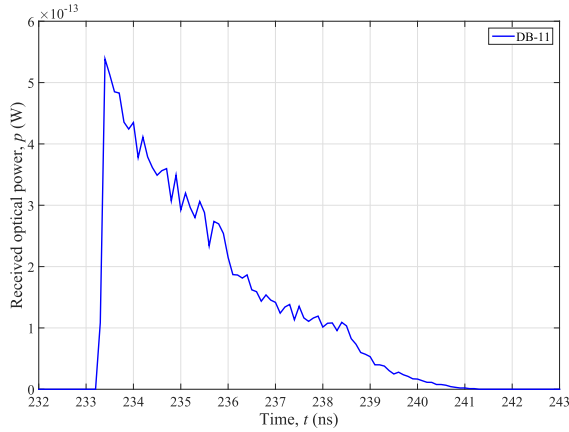


Fig. 9. Received power from DB – 11 component within the two-ring model ($t = 0$, $D = 70$ m).

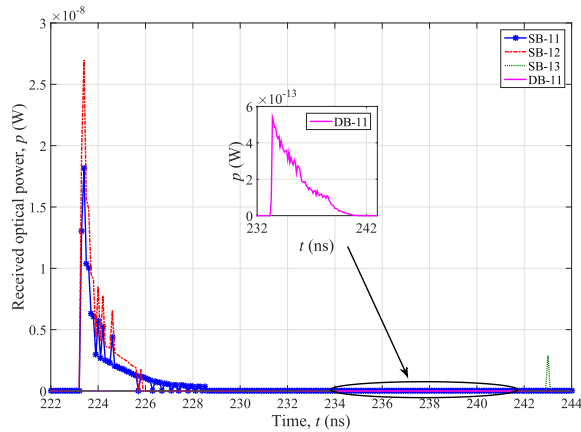


Fig. 10. Received power from SB – 11, SB – 12, SB – 13, and DB – 11 components for the combined two-ring model and ellipse model ($t = 0$, $D = 70$ m).

based on the initial distance only, i.e., $t = 0$ and $D = 70$ m. Compared with SB components, it can be noticed that the DB component carry a significantly smaller amount of power. It is worthwhile to mention that there are another probable optical paths can be double bounced within the proposed model as detailed in [25] for indoor VLC. For instance, one probable path can be scattered by the scatterers on the Tx-ring then reflected off by the scatterers on the ellipse. In this study, such paths are not considered because they will be highly attenuated and have insignificant contribution to the total power that arrives the PD. Although DB – 11 component carries insufficient power, it comes earlier than SB – 13 as it is clearly shown in Fig. 10. This is due to the shorter path length in the two-ring model. The SB and DB components of the CIR are shown in Fig. 10. However, for VLC, the first reflection is the most important component which limits the data rates. Late components show more dispersive channel characteristics resulting in high delay spread, and hence low channel bandwidth.

The previous discussion was based on the static condition assumption, i.e., $t = 0$ and $D = 70$ m. Let's consider the dynamic condition in which both Tx and Rx are moving in the

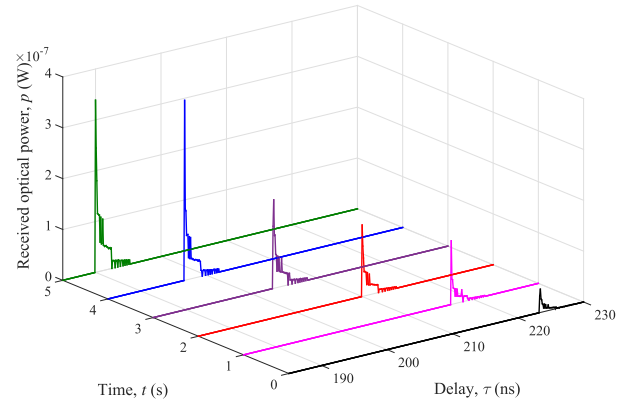


Fig. 11. Received power from SB – 11 and SB – 12 component (the Tx and Rx are moving, $v_{Tx} = 21.6$ km/h, $v_{Rx} = 14.4$ km/h, $t = 0 - 5$ s).

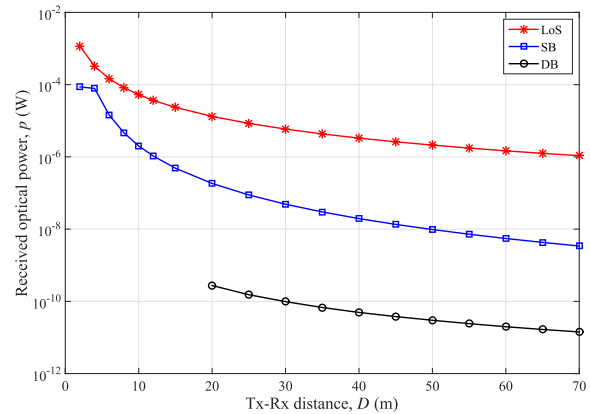


Fig. 12. The received optical power from LoS, SB, and DB components.

same direction with different speeds as detailed in Table III. In terms of SB components in the two-ring model, Fig. 11 shows the contribution of the two-ring model when both the Tx and Rx are moving according to (9) and (10). Here the total power of both SB – 11 and SB – 12 is considered at specific times. Since the Tx vehicle is moving relatively faster than target Rx vehicle, the received power increases gradually. In this case, the optical path lengths and both AoD and AoA are the main parameters which are effects signal strength.

On the other hand, in terms of the DB component of the CIR in the dynamic mode, simulation results have demonstrated that the received power between 2.7×10^{-10} W and 1.4×10^{-11} W, which are corresponding to Tx-Rx distance 20 m and 70 m, respectively. The former distance represents the minimum distance to maintain DB reflection between two cars. In order to summarize above discussions regarding received power, Fig. 12 illustrates the relationships between the received optical powers from LoS, SB, and DB components with Tx-Rx distances. The results are calculated based on applying (7), (9), (10), and (24) using the parameters given in Table III when the PD is mounted at 0.6 m height.

Since it has been demonstrated that DB components are insufficient enough to be used for further analysis, the rest of this paper will focus on SB components.

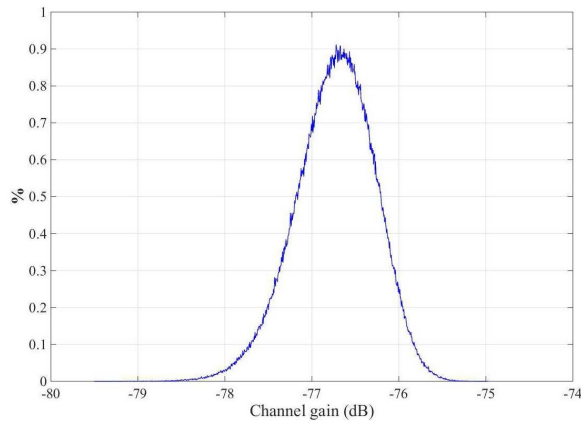


Fig. 13. Channel gain (dB) for SB components in two-ring model.

B. VVLC Channel Gain

The understanding of GBSM requires some basic knowledge about the statistical properties of the proposed channel model, such as channel gain and RMS delay spread. The received signal consists of various components arriving from different paths. The path lengths of these components differ in proportion to the scatterers' distribution. Therefore, the main concern is the fitting of the statistical properties of the proposed channel models to the statistics of real-world channels.

In terms of channel gain in dB, let us now evaluate the mean channel gain and the distribution of channel gain at a particular distance, specifically 70 m. In this regard, based on simulation data we will investigate propagation characteristics for a large ensemble of scatterers locations with different angular distributions. Consequently, the resultant channel gain distribution for the SB components in the two-ring model is illustrated in Fig. 13. It can be noticed that the mean channel gain is -76.73 dB.

In respect of analyzing the resultant channel gain distribution in Fig. 13, we can notice that the most potential distribution that fit the results is the Gaussian distribution. To evaluate the channel model at the given distance, two methods have been used. First, we performed a cumulative distribution function (CDF) fitting method for the resultant distribution. A Monte Carlo simulation of 10^6 iterations (realizations) is carried out. In each realization, the value of the AoD/AoA is randomly generated following a uniform distribution. The resultant distribution is then verified by applying empirical CDF technique, which is a built-in function in MATLAB. The CDF fitting result is illustrated in Fig. 14. Here, we can notice that the CDF fitting method produces a good fit across all the channel gain samples. Second, we use the χ^2 -goodness-of-fit test [40]. The χ^2 -test is generally used to test the hypothesis that a function $F(x)$ is the distribution of the sample population x_1, x_2, \dots, x_n . If the sample population deviates too much from $F(x)$ then that hypothesis will be rejected. Here, we will perform the test on all groups of data for the distribution that obtained from SB components in the two-ring model. The result of the

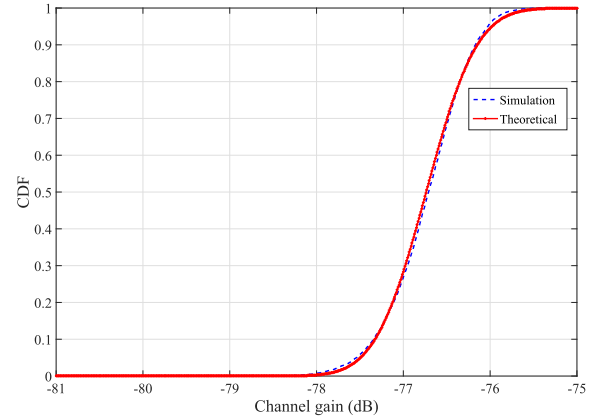


Fig. 14. CDF fitting for simulation results of VVLC channel gain.

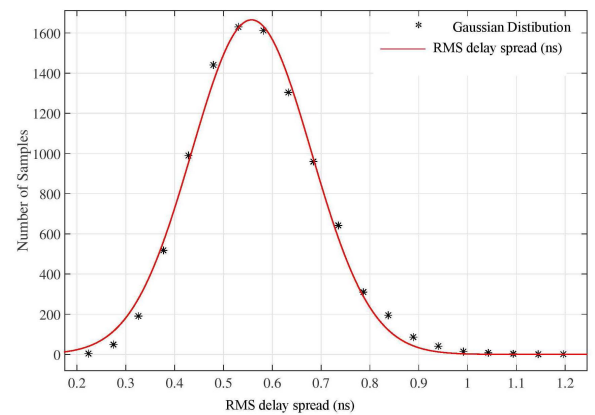


Fig. 15. Curve fitting of channel RMS delay spread histogram for SB components in the two-ring model.

simulation is analyzed using χ^2 -goodness-of-fit test built-in function in MATLAB. According to that function, the test result is denoted by $\chi^2_{.05}$, which means that the null hypothesis has been estimated at the 5% significance level. Consequently, if $\chi^2_{.05}$ is 1, the test rejects the null hypothesis, while if the returned value $\chi^2_{.05} = 0$, that means the test does not reject the null hypothesis at the default 5% significance level. Based on our simulation results, examining the normal distribution has passed the χ^2 -test. In terms of results validation, it is worth mentioning that comparable results have been obtained in [31].

C. RMS Delay Spread

By following the same methodology which is used in Section V-B, in this subsection, the RMS delay spread model for the SB channels is developed. Here, Gaussian distribution has been examined again to model the RMS delay spread D_{rms} of VVLC channels. In this context, Gaussian distribution has passed the χ^2 -test firstly. Secondly, we used the probability density function (PDF) fitting method to characterize the results with the theoretical PDF of Gaussian distribution as illustrated in Fig. 15. The last figure shows that the Gaussian is a good estimate for RMS delay spread of SB components.

VI. CONCLUSIONS

VLC technology has been considered as an alternative and complementary to RF wireless communications for both indoor and outdoor applications. Therefore, in this paper, the potential of using VLC technology in vehicular communications has been investigated. A RS-GBSM combining the two-ring and confocal ellipse models has been adopted to model VVLC channels. VVLC channel characteristics have been investigated through a large set of channel impulse responses generated from the proposed RS-GBSM. The received optical powers for LoS, SB, and DB components have been computed along different distance ranges between 0 and 70 m. Furthermore, the LoS received power has been obtained when the PD is mounted at three different heights. In terms of SB components, the traditional fitting methods have confirmed that the Gaussian distributions are the best fit for channel gain in dB and RMS delay spread. Finally, the results have indicated that the DB components carry inconsiderable optical power.

REFERENCES

- [1] World Health Organization. *Road Traffic Injuries*. Accessed: Oct. 14, 2018. [Online]. Available: <http://www.who.int/mediacentre/factsheets/fs358/en/>
- [2] Z. Ghassemlooy, L. N. Alves, S. Zvanovec, and M.-A. Khalighi, *Visible Light Communications: Theory and Applications*. New York, NY, USA: CRC Press, 2017.
- [3] *Annual Global Road Crash Statistics*. Accessed: Oct. 14, 2018. [Online]. Available: <http://www.asirt.org/initiatives/informing-road-users/road-safety-facts/road-crash-statistics>
- [4] J.-H. Yoo, J.-S. Jang, J. K. Kwon, H.-C. Kim, D.-W. Song, and S.-Y. Jung, "Demonstration of vehicular visible light communication based on LED headlamp," *Int. J. Automot. Technol.*, vol. 17, no. 2, pp. 347–352, Apr. 2016.
- [5] S. Dimitrov and H. Haas, *Principles of LED Light Communications: Towards Networked Li-Fi*. London, U.K.: Cambridge Univ. Press, 2015.
- [6] C.-X. Wang *et al.*, "Cellular architecture and key technologies for 5G wireless communication networks," *IEEE Commun. Mag.*, vol. 52, no. 2, pp. 122–130, Feb. 2014.
- [7] C.-X. Wang, X. Cheng, and D. I. Laurenson, "Vehicle-to-vehicle channel modeling and measurements: Recent advances and future challenges," *IEEE Commun. Mag.*, vol. 47, no. 11, pp. 96–103, Nov. 2009.
- [8] X. Ge *et al.*, "Wireless fractal cellular networks," *IEEE Wireless Commun. Mag.*, vol. 23, no. 5, pp. 110–119, Oct. 2016.
- [9] M. Uysal, C. Capsoni, Z. Ghassemlooy, A. Boucouvalas, and E. G. Udvary, *Optical Wireless Communications: An Emerging Technology*. Bern, Switzerland: Springer, 2016.
- [10] European Commission. *Daytime Running Lights*. Accessed: Oct. 14, 2018. [Online]. Available: <https://ec.europa.eu/transport/road-safety/topics/vehicles/daytime-running-lights>
- [11] I. Knight, B. Sexton, R. Bartlett, T. Barlow, S. Latham, and I. Mcrae. (Jan. 2007). *Daytime Running Lights (DRL): A Review of the Reports From the European Commission*. [Online]. Available: <http://www.gov.uk/government/organisations/department-for-transport>
- [12] X. Cheng, C.-X. Wang, B. Ai, and H. Aggoune, "Envelope level crossing rate and average fade duration of nonisotropic vehicle-to-vehicle Ricean fading channels," *IEEE Trans. Intell. Transp. Syst.*, vol. 15, no. 1, pp. 62–72, Feb. 2014.
- [13] X. Cheng, C.-X. Wang, D. I. Laurenson, S. Salous, and A. V. Vasilakos, "An adaptive geometry-based stochastic model for non-isotropic MIMO mobile-to-mobile channels," *IEEE Trans. Wireless Commun.*, vol. 8, no. 9, pp. 4824–4835, Sep. 2009.
- [14] Y. Yuan, C.-X. Wang, X. Cheng, B. Ai, and D. I. Laurenson, "Novel 3D geometry-based stochastic models for non-isotropic MIMO vehicle-to-vehicle channels," *IEEE Trans. Wireless Commun.*, vol. 13, no. 1, pp. 298–309, Jan. 2014.
- [15] S. Wu, C.-X. Wang, E.-H. M. Aggoune, M. M. Alwakeel, and X. You, "A general 3-D non-stationary 5G wireless channel model," *IEEE Trans. Commun.*, vol. 66, no. 7, pp. 3065–3078, Jul. 2018.
- [16] C.-X. Wang, J. Bian, J. Sun, W. Zhang, and M. Zhang, "A survey of 5G channel measurements and models," *IEEE Commun. Surveys Tuts.*, vol. 20, no. 4, 4th Quart., 2018.
- [17] Z. Ghassemlooy, W. Popoola, and S. Rajbhandari, *Optical Wireless Communications: System and Channel Modelling With MATLAB*, 1st ed. New York, NY, USA: CRC Press, 2013.
- [18] H. Elgala, R. Mesleh, and H. Haas, "Practical considerations for indoor wireless optical system implementation using OFDM," in *Proc. ConTEL*, Zagreb, Croatia, Jun. 2009, pp. 25–29.
- [19] M. Wada, T. Yendo, T. Fujii, and M. Tanimoto, "Road-to-vehicle communication using LED traffic light," in *Proc. IEEE Intell. Vehicles Symp.*, Las Vegas, NV, USA, Jun. 2005, pp. 601–606.
- [20] G. Pang, T. Kwan, H. Liu, and C.-H. Chan, "LED wireless," *IEEE Ind. Appl. Mag.*, vol. 8, no. 1, pp. 21–28, Jan. 2002.
- [21] S. J. Lee, J. K. Kwon, S. Y. Jung, and Y. H. Kwon, "Simulation modeling of visible light communication channel for automotive applications," in *Proc. IEEE ITSC*, Anchorage, AK, USA, Sep. 2012, pp. 463–468.
- [22] S. Lee, J. K. Kwon, S.-Y. Jung, and Y.-H. Kwon, "Evaluation of visible light communication channel delay profiles for automotive applications," *EURASIP J. Wireless Commun. Netw.*, vol. 10, no. 11, p. 370, 2012.
- [23] P. Luo, Z. Ghassemlooy, H. Le Minh, E. Bentley, A. Burton, and X. Tang, "Performance analysis of a car-to-car visible light communication system," *Appl. Opt.*, vol. 54, no. 7, pp. 1696–1706, Mar. 2015.
- [24] A. Al-Kinani, C.-X. Wang, H. Haas, and Y. Yang, "Characterization and modeling of visible light communication channels," in *Proc. IEEE VTC*, Nanjing, China, May 2016, pp. 1–5.
- [25] A. Al-Kinani, C.-X. Wang, H. Haas, and Y. Yang, "A geometry-based multiple bounce model for visible light communication channels," in *Proc. IEEE IWCMC*, Paphos, Cyprus, Sep. 2016, pp. 31–37.
- [26] A. Al-Kinani, C.-X. Wang, L. Zhou, and W. Zhang, "Optical wireless communication channel measurements and models," *IEEE Commun. Surveys Tuts.*, vol. 20, no. 3, pp. 1939–1962, 3rd Quart., 2018.
- [27] F. R. Gfeller and U. Bapst, "Wireless in-house data communication via diffuse infrared radiation," *Proc. IEEE*, vol. 67, no. 11, pp. 1474–1486, Nov. 1979.
- [28] Y. A. Alqudah and M. Kavehrad, "MIMO characterization of indoor wireless optical link using a diffuse-transmission configuration," *IEEE Trans. Commun.*, vol. 51, no. 9, pp. 1554–1560, Sep. 2003.
- [29] J. R. Barry, *Wireless Infrared Communications*. New York, NY, USA: Springer, 1994.
- [30] J. R. Barry, J. M. Kahn, W. J. Krause, E. A. Lee, and D. G. Messerschmitt, "Simulation of multipath impulse response for indoor wireless optical channels," *IEEE J. Sel. Areas Commun.*, vol. 11, no. 3, pp. 367–379, Apr. 1993.
- [31] J. B. Carruthers and S. M. Carroll, "Statistical impulse response models for indoor optical wireless channels," *Int. J. Commun. Syst.*, vol. 18, pp. 267–284, Apr. 2005.
- [32] B. Schoettle and M. J. Flannagan, "A market-weighted description of low-beam and high-beam headlighting patterns in the U.S.," *Transp. Res. Inst., Univ. Michigan*, Ann Arbor, MI, USA, Tech. Rep. UMTRI-2004-23, 2004.
- [33] M. Pätzold, *Mobile Radio Channels*, 2nd ed. Chichester, U.K.: Wiley, 2012.
- [34] M. D. A. Mohamed and S. Hranilovic, "Optical impulse modulation for indoor diffuse wireless communications," *IEEE Trans. Commun.*, vol. 57, no. 2, pp. 499–508, Feb. 2009.
- [35] D. Wu, Z. Ghassemlooy, H. L. Minh, S. Rajbhandari, and A. C. Boucouvalas, "Improvement of the transmission bandwidth for indoor optical wireless communication systems using a diffused Gaussian beam," *IEEE Commun. Lett.*, vol. 16, no. 8, pp. 1316–1319, Aug. 2012.
- [36] Transport Canberra and City Services. (Mar. 17, 2016). *Design Standards for Urban Infrastructure*. Accessed: Feb. 5, 2018. [Online]. Available: <https://www.tccs.act.gov.au/>
- [37] Alta Planning and Design, Cambridge, MA, USA. (Jan. 2017). *Urban, Rural and Suburban Complete Streets Design Manual*. Accessed: Feb. 5, 2018. [Online]. Available: <https://www.northamptonma.gov/DocumentCenter/View/6668>
- [38] M. Fabian, E. Lewis, T. Newe, and S. Lochmann, "Optical fibre cavity for ring-down experiments with low coupling losses," *Meas. Sci. Technol.*, vol. 21, p. 094034, Jul. 2010.
- [39] M. L. Marceau and M. G. VanGeem. (Aug. 2008). *Solar Reflectance Values of Concrete*. Springfield, IL, USA. Accessed: Mar. 1, 2018. [Online]. Available: <http://www.cement.org>
- [40] B. M. Ayyub and R. H. McCuen, *Probability & Statistics for Engineers & Scientists*, 1st ed. Boca Raton, FL, USA: CRC Press, 1997.



Ahmed Al-Kinani received the B.Sc. degree (Hons.) in laser physics and the M.Sc. degree in optical communications from the University of Technology, Baghdad, Iraq, in 2001 and 2004, respectively, and the Ph.D. degree in optical wireless communications from The University of Edinburgh and Heriot-Watt University, Edinburgh, U.K., in 2018. He is currently with the Iraqi Ministry of Communications, Baghdad, as a Senior Programmer. His main research interests include wireless channel characterization and modeling for visible light communications.

He was a recipient of the Best Paper Award from IWCMC 2016.



Jian Sun (M'08) received the B.Sc. degree in applied electronic technology, the M.Eng. degree in measuring and testing technologies and instruments, and the Ph.D. degree in communication and information systems from Zhejiang University, Hangzhou, China, in 1996, 1999, and 2005, respectively. In 2011, he was a Visiting Scholar with Heriot-Watt University, U.K., supported by U.K.-China Science Bridges: Research and Development on (B)4G Wireless Mobile Communications (UC4G) Project. Since 2005, he has been a Lecturer with the

School of Information Science and Engineering, Shandong University, China. His current research interests are in the areas of signal processing for wireless communications, channel sounding and modeling, propagation measurement and parameter extraction, and MIMO and multicarrier transmission systems design and implementation.



Cheng-Xiang Wang (S'01-M'05-SM'08-F'17) received the B.Sc. and M.Eng. degrees in communication and information systems from Shandong University, China, in 1997 and 2000, respectively, and the Ph.D. degree in wireless communications from Aalborg University, Denmark, in 2004.

He was a Research Assistant with the Hamburg University of Technology, Hamburg, Germany, from 2000 to 2001, a Research Fellow with the University of Agder, Grimstad, Norway, from 2001 to 2005, and a Visiting Researcher with Siemens AG-Mobile

Phones, Munich, Germany, in 2004. He has been with Heriot-Watt University, Edinburgh, U.K., since 2005, where he became a Professor in wireless communications in 2011. In 2018, he joined Southeast University, Nanjing, China, as a Professor. He has co-authored two books, one book chapter, and over 340 papers in refereed journals and conference proceedings. His current research interests include wireless channel measurements/modeling and (B)5G wireless communication networks, including green communications, cognitive radio networks, high mobility communication networks, massive MIMO, millimeter wave communications, and visible light communications.

Dr. Wang is a fellow of the IET and HEA. He was a recipient of nine Best Paper Awards from the IEEE GLOBECOM 2010, IEEE ICCT 2011, ITST 2012, IEEE VTC 2013-Spring, IWCMC 2015, IWCMC 2016, IEEE/CIC ICC 2016, and WPMC 2016. He was also recognized as a Highly Cited Researcher by Web of Science in 2017. He has served as a technical program committee (TPC) member, the TPC chair, and the general chair for over 80 international conferences. He was a Guest Editor for the IEEE JOURNAL ON SELECTED AREAS IN COMMUNICATIONS Special Issue on Spectrum and Energy Efficient Design of Wireless Communication Networks and the Special Issue on Airborne Communication Networks, and the IEEE TRANSACTIONS ON BIG DATA Special Issue on Wireless Big Data. He has served as an Editor for nine international journals including the IEEE TRANSACTIONS ON WIRELESS COMMUNICATIONS from 2007 to 2009. He has also served as an Editor for the IEEE TRANSACTIONS ON VEHICULAR TECHNOLOGY since 2011 and the IEEE TRANSACTIONS ON COMMUNICATIONS since 2015. He was a Lead Guest Editor of the IEEE JOURNAL ON SELECTED AREAS IN COMMUNICATIONS Special Issue on Vehicular Communications and Networks.



Wensheng Zhang (S'08-M'11) received the M.E. degree in electrical engineering from Shandong University, China, in 2005, and the Ph.D. degree in electrical engineering from Keio University, Japan, in 2011. In 2011, he was a Visiting Researcher with Oulu University, Finland. He was an Assistant Professor with the School of Communication, Shandong Normal University, China, from 2005 to 2007. In 2012, he joined the School of Information Science and Engineering, Shandong University, where he is currently an Associate Professor. His research

interests lie in random matrix theory, cognitive radio networks, visible light communications, and 5G wireless communications.



Xiaohu Ge (M'09-SM'11) received the Ph.D. degree in communication and information engineering from Huazhong University of Science and Technology (HUST) in 2003. He was a Researcher with Ajou University, South Korea, and the Politecnico Di Torino, Italy, from 2004 to 2005. He is currently a Full Professor with the School of Electronic Information and Communications, HUST, China. He is also an Adjunct Professor with the Faculty of Engineering and Information Technology, University of

Technology Sydney, Australia. His research interests are in the areas of mobile communications, traffic modeling in wireless networks, green communications, and interference modeling in wireless communications. He has published over 200 papers in refereed journals and conference proceedings. He held about 25 patents in China. He has received the Best Paper Award from the IEEE GLOBECOM 2010. He served as the General Chair of the 2015 IEEE International Conference on Green Computing and Communications (IEEE GreenCom 2015). He serves as an Associate Editor for the IEEE WIRELESS COMMUNICATIONS, the IEEE TRANSACTIONS ON VEHICULAR TECHNOLOGY, and the IEEE ACCESS.



Harald Haas (S'98-A'00-M'03-SM'16-F'18) received the Ph.D. degree from The University of Edinburgh in 2001. His main research interests are in optical wireless communications, hybrid optical wireless and RF communications, spatial modulation, and interference management in wireless networks. In 2014, he was selected by EPSRC as one of the ten Recognising Inspirational Scientists and Engineers or Leaders in the U.K. He is currently the Chair of mobile communications with The University of Edinburgh, the Founder

and Chief Scientific Officer of pureLiFi Ltd., and the Director of the LiFi Research and Development Center, The University of Edinburgh. He first introduced and coined spatial modulation and LiFi. LiFi was listed among the 50 best inventions in *Time* magazine in 2011. He was an invited speaker with TED Global 2011, and his talk on Wireless Data from Every Light Bulb has been watched online over 2.5 million times. He gave a second TED Global talk in 2015 on the use of solar cells as LiFi data detectors and energy harvesters. This has been viewed online over 2.0 million times. He has published over 400 conference and journal papers including a paper in science. He has co-authored a book entitled *Principles of LED Light Communications Towards Networked Li-Fi* (Cambridge University Press) in 2015. He was elected as a Fellow of the Royal Society of Edinburgh in 2017. He was a co-recipient of the Best Paper Awards from VTC-Fall 2013, VTC-Spring 2015, ICC 2016, and ICC 2017. He was also a co-recipient of the EURASIP Best Paper Award for the *Journal on Wireless Communications and Networking* in 2015 and the Jack Neubauer Memorial Award of the IEEE Vehicular Technology Society. In 2012 and 2017, he was a recipient of the Prestigious Established Career Fellowship from the Engineering and Physical Sciences Research Council (EPSRC). He is currently an Associate Editor for the IEEE/OSA JOURNAL OF LIGHTWAVE TECHNOLOGIES. In 2016, he received the Outstanding Achievement Award from the International Solid State Lighting Alliance.